Activation of C-H bonds by a nonheme iron(IV)-oxo complex: mechanistic evidence through a coupled EDXAS/UV-Vis multivariate analysis

Francesco Tavani,[a,*] Giorgio Capocasa,[a] Andrea Martini,[b,c] Francesco Sessa,[a] Stefano Di Stefano,[a] Osvaldo Lanzalunga[a] and Paola D'Angelo[a,*]

[a] Dipartimento di Chimica, Università di Roma "La Sapienza", P.le A. Moro 5, 00185 Roma, Italy.

[b] Dipartimento di Chimica, Università degli Studi di Torino, Via P. Giuria 7, 10125 Torino, Italy.

[c] The Smart Materials Research Institute, Southern Federal University, 344090 Sladkova 178/24 Rostov-on-Don, Russia.

[*] p.dangelo@uniroma1.it, francesco.tavani@uniroma1.it

Abstract

The understanding of reactive processes involving organic substrates is crucial to chemical knowledge and requires multidisciplinary efforts for its advancement. Herein, we apply a combined multivariate, statistical and theoretical analysis of coupled time-resolved X-ray absorption (XAS)/ UV-Vis data to obtain detailed mechanistic information for the C-H bond activation of 9,10-dihydroanthracene (DHA) and diphenylmethane (Ph_2CH_2) by the nonheme Fe^{IV}-oxo complex $[N4Py{\cdot}Fe^{IV}(O)]^{2+}$ (N4Py = *N*,*N*-bis(2-pyridylmethyl)-*N*-bis(2-pyridyl)methylamine) in CH_3CN at room temperature. Within this approach, we determine the number of key chemical species present in the reaction mixtures and derive spectral and concentration profiles for the reaction intermediates. From the quantitative analysis of

the XAS spectra the transient intermediate species are structurally determined. As a result, it is suggested that, while DHA is oxidized by [N4Py·Fe^{IV}(O)]$^{2+}$ with a hydrogen atom transfer-electron transfer (HAT-ET) mechanism, Ph_2CH_2 is oxidized by the nonheme iron-oxo complex through a HAT-radical dissociation pathway. In the latter process, we prove that the intermediate Fe^{III} complex [N4Py·Fe^{III}(OH)]$^{2+}$ is not able to oxidize the diphenylmethyl radical and we provide its structural characterization in solution. The employed combined experimental and theoretical strategy is promising for the spectroscopic characterization of transient intermediates as well as for the mechanistic investigation of redox chemical transformations on the second to millisecond time scales.

1 Introduction

Heme and nonheme Fe^{IV}-oxo complexes play an important role in a wide variety of reactions, including alkane hydroxylation.[1,2] In biological systems, the accepted mechanism for alkane hydroxylation is that of an initial hydrogen abstraction (HAT) by the Fe(O) high-valent species followed by an oxygen rebound (OR) process between the formed substrate radical and the resulting FeOH complex.[3,4] Also in nonheme systems a HAT-OR mechanism has been suggested for the activation of C-H bond containing alkanes, leading the complex to a final Fe^{II} oxidation state.[1,5–8] In some cases, the possibility of forming alkene products has been observed.[9–11] However, there have been reports suggesting the HAT-OR mechanism is not the only active one.[12,13] Notably, it has been shown through theoretical and experimental evidence that the hydroxylation of a series of alkanes by [(Bn-TPEN)-Fe^{IV}(O)]$^{2+}$ and [N4Py·Fe^{IV}(O)]$^{2+}$ occurs preferably through a dissociation of the substrate radical (RD), previously formed via HAT, as opposed to the oxygen rebound or desaturation pathways.[2] According to this mechanistic hypothesis, it was shown by a combination of electron paramagnetic resonance (EPR) and electrospray ionization (ESI) mass spectrometry analyses of the reaction solutions that the Fe^{III} species [N4Py·Fe^{III}(OH)]$^{2+}$ was formed as a final product during the process, a conclusion further supported by the conversion of the UV-Vis silent Fe^{III} end product to Fe^{II} upon reduction with ferrocene.[2] However, to the best of our knowledge, neither the Fe^{III}-OH intermediate concentration time evolution during the reactive process has been quantitatively determined nor has the structure of the same species been characterized.

Time-resolved spectroscopic monitoring of chemical processes has been widespread and essential for the investigation of their underlying mechanisms. Among the more common laboratory-based spectroscopic techniques, energy dispersive X-ray absorption spectroscopy (EDXAS) sets itself apart as an advanced tool to follow reactions occurring on the second to millisecond time scales. Notably, EDXAS offers the possibility of gaining simultaneous information on the time evolution of the oxidation state of the given photoabsorber and of its molecular surroundings within 5 Å with a good degree of accuracy.[14–16] We have recently applied this technique in combination with UV-Vis spectroscopy for the identification of the succession of oxidation states and for the measurement of pseudo-first-order kinetic constants in bimolecular reactions involving nonheme iron complexes.[14,15,17]
Herein, we combine multivariate statistical and theoretical analyses of time-resolved coupled EDXAS/UV-Vis data to gain a comprehensive mechanistic picture on the activation of C-H bonds in the substrates 9,10-dihydroanthracene (DHA) and diphenylmethane (Ph_2CH_2) by the nonheme Fe^{IV}-oxo complex $[N4Py{\cdot}Fe^{IV}(O)]^{2+}$. In particular, quantitative mechanistic and structural information for all the reaction intermediates is derived from the application of principal component analysis (PCA) and a strategy belonging to the multivariate curve resolution (MCR) family. Through the employed method the measured spectroscopic signal is decomposed into a set of N uncorrelated spectra associated to the reaction key species and into the set of their relative concentrations.[18] The use of MCR for the study of X-ray absorption near edge structure (XANES) time-resolved data relative to chemical transformations is a relatively new development,[16] while there have been in the past numerous applications of PCA to this end. For example, biochemical reactions,[19,20] and phase speciation for an heterogeneous mixture of Co organometallic species were investigated by means of PCA together with multiple data set fits of the extended X-ray absorption fine structure(EXAFS) region and residual phase analysis. Further, the structures and the time evolution of the concentrations belonging to the intermediates of a reaction involving a methylrhenium trioxide catalyst in solution were obtained by combining PCA, XANES anlysis and multidimensional interpolation of theoretical XANES spectra as a function of structural parameters.[21] Conversely, chemical systems so far mainly in the solid phase are being increasingly studied by means of the MCR algorithm, such as doped V_2O_5 lithium batteries,[22] the effect of heating on the decomposition of chlorine layered double hydroxide (LDH),[23] Cu reducibility and speciation in Cu-CHA zeolite catalysts,[24,25]

and chemical transformations involved in other solid state processes.[26–32] The synergistic application of interdisciplinary spectroscopic and theoretical techniques holds promise for the study of chemical reactions occurring on the second to millisecond time scales as demonstrated by the successful application to the investigation of the activation processes of nonheme iron complexes and of the oxidation of aromatic sulfides promoted by nonheme Fe^{IV}-oxo complexes.[16,33] In this work we show that the coupled XAS/UV-Vis multivariate analysis can be applied profitably to the mechanistic analysis of the most important reaction promoted by nonheme Fe^{IV}-oxo complexes, i.e. the C-H activation of hydrocarbons.

2 Method

We investigated the oxidation reactions of DHA and Ph_2CH_2 by $[N4Py{\cdot}Fe^{IV}(O)]^{2+}$ in CH_3CN at 25 °C, with the iron-oxo complex formed by reaction of the Fe(II) complex with peroxyacetic acid (AcOOH) (220 mM, added as a 36-40 % w/w AcOH stock solution). Both processes were run under pseudo-first-order conditions (DHA 45 mM and Ph_2CH_2 300 mM, respectively, added to $[N4Py{\cdot}Fe^{IV}(O)]^{2+}$ 8 mM). The concentration of the substrates was chosen in order to ensure their complete solubility and to keep the reaction time within the limits dictated by the experimental set-up.

2.1 Decomposition of UV-Vis and EDXAS data into the spectra and fractional concentrations of key components

Time-resolved spectroscopical measurements of chemical processes yield a series of spectra that may be positioned in a matrix $\boldsymbol{D}$, where the columns of $\boldsymbol{D}$ are the spectra measured at time t. According to Lambert-Beer's law, at any given time from reaction start a number N of "pure" and independent components weighed by their fractional concentration contributes to the measured signal.[18] Decomposing the experimental data into the spectra associated to the key reaction species and into their relative concentration profiles can offer important insight into the reaction mechanism. In the present work, such decomposition was performed with the PyFitit code,[18] a software that uses to such end an algorithm belonging to the MCR family.[34]

The starting point of the employed approach is the Singular Value Decomposition (SVD) equation:

$$\boldsymbol{D} = \boldsymbol{U} \cdot \boldsymbol{\Sigma} \cdot \boldsymbol{V} + \boldsymbol{E} \tag{1}$$

where the product $\boldsymbol{U} \cdot \boldsymbol{\Sigma}$ contains, on its N columns, a set of values that may be associated to the normalized absorption coefficients, $\boldsymbol{\Sigma}$ is a diagonal matrix known as the *singular value* term, whose elements are sorted in decreasing order, while $\boldsymbol{V}$ can be interpreted as the concentration matrix associated to the N-selected components. Lastly, the error matrix $\boldsymbol{E}$ represents the lack of fit between the experimental data matrix $\boldsymbol{D}$ and the reconstructed matrix $\boldsymbol{\mu} = \boldsymbol{U} \cdot \boldsymbol{\Sigma} \cdot \boldsymbol{V}$. The SVD deconvolution depends on the correct estimation of the number of components N present in the experimental spectral matrix. This may be achieved by combining different statistical tests and empirical evidences.[18] Among them, in this work we chose to use the scree plot and Imbedded-Error (IE) function analyses since they are readily interpreted (further discussed in Section 2.6 of the ESI).
At this point, all matrices in eq. 1 are solely mathematical solutions to the decomposition problem without physico-chemical meaning. Once N is established, the approach implemented by PyFitIt requires the introduction of a N × N transformation matrix $\boldsymbol{T}$ in eq. 1, using the relation $\boldsymbol{I} = \boldsymbol{T} \cdot \boldsymbol{T}^{-1}$:

$$\boldsymbol{D} = \boldsymbol{U} \cdot \boldsymbol{\Sigma} \cdot \boldsymbol{T} \cdot \boldsymbol{T}^{-1} \cdot \boldsymbol{V} + \boldsymbol{E} \tag{2}$$

where the spectra belonging to the key reaction species are given by $\boldsymbol{S} = \boldsymbol{U} \cdot \boldsymbol{\Sigma} \cdot \boldsymbol{T}$ and their concentration profiles by $\boldsymbol{C} = \boldsymbol{T}^{-1} \cdot \boldsymbol{V}$. Subsequently, the matrix elements T_{ij} of matrix $\boldsymbol{T}$ are modified by sliders to achieve $\boldsymbol{S}$ and $\boldsymbol{C}$ which are chemically and physically interpretable. Once this step is achieved, one can finally write:

$$\boldsymbol{D} = \boldsymbol{S} \cdot \boldsymbol{C} + \boldsymbol{E} \tag{3}$$

The unknown number of T_{ij} elements of $\boldsymbol{T}$ is in principle equal to N^2. In order to reduce such ambiguity, some constraints were imposed. In the case of the analyses of the UV-Vis data for both reactions, the transformation matrix elements were varied in order to extract spectral components in accord with the UV-Vis spectra known to belong to the reaction species. At wavelenghts superior to 513 nm, the UV-Vis spectrum of complex $[\mathrm{N4Py{\cdot}Fe}^{II}(\mathrm{CH_3CN})]^{2+}$

is comprised of the shoulder of a transition centered at $\lambda = 495$ nm. In that same spectral range, the UV-Vis spectrum of complex [N4Py·Fe^{IV}(O)]$^{2+}$ is constituted by a broad peak centered at approximately $\lambda = 695$ nm. The spectra of these two species are shown in Fig. S5. Lastly, complex [N4Py·Fe^{III}(OH)]$^{2+}$, exhibits a very weak, if any, absorbance in this spectral range.[2,35]

In the case of the DHA reaction, a 2×2 matrix $\boldsymbol{A_1}$ was defined containing four elements. The solution for the decomposition presented in eq. 3 was obtained using the following matrix:

$$\boldsymbol{A_1} = \begin{pmatrix} -0.298 & -0.168 \\ +0.082 & -3.198 \end{pmatrix} \tag{4}$$

Conversely, the following 3×3 matrix $\boldsymbol{A_2}$ was defined, containing nine elements, to decompose the UV-Vis data relative to the Ph_2CH_2 reaction:

$$\boldsymbol{A_2} = \begin{pmatrix} -0.0011 & -0.0090 & -0.0110 \\ -0.0019 & +0.0070 & -0.0468 \\ -0.0520 & +0.0342 & +0.0274 \end{pmatrix} \tag{5}$$

In the case of the decomposition of the EDXAS dataset relative to the Ph_2CH_2 oxidation, the normalization of all spectral components contained in matrix $\boldsymbol{S}$ was required. This procedure reduces the unknown number of the transformation matrix elements from N^2 to $N^2 - N$. The solution for the decomposition was obtained using the following 3×3 matrix $\boldsymbol{A_3}$:

$$\boldsymbol{A_3} = \begin{pmatrix} 1/\sigma & 1/\sigma & 1/\sigma \\ +0.120 & -0.220 & -0.180 \\ +0.100 & -0.420 & +0.370 \end{pmatrix} \tag{6}$$

where $\sigma = 0.0869$ is the normalization coefficient.

For all analyses the non-negativity of both UV-Vis and XANES extracted spectral and concentration profiles was implemented by looking for a set of parameters capable of furnishing absorption and concentration profiles that were non-negative.[18,36] For the detailed explanation of how these constraints are imposed, see Ref.[18]

3 Results and discussion

Fig. 1 presents the UV-Vis time course of the reaction of DHA with [N4Py·Fe^{IV}(O)]$^{2+}$ followed through the absorbance decrease due to the decay of [N4Py·Fe^{IV}(O)]$^{2+}$

($\lambda = 695$ nm) and the absorbance increase due to the buildup of $[\text{N4Py}\cdot\text{Fe}^{II}(\text{CH}_3\text{CN})]^{2+}$ ($\lambda = 513$ nm). These spectroscopic data were subjected to two statistical tests in order to determine the number of chemical species contributing to the total measured signal. In particular, a scree plot and an IE-function test were performed (refer to Section 2.6 of the ESI for additional details).[18,36,37] The presence of an elbow in the scree plot between the second and third Principal Component (PC) (Fig. 2a), as well as the fact that the IE-function is minimized by N = 2 suggest that there are two active species contributing to the UV-Vis spectra (Fig. 2c).

Conversely, Fig. 3 presents the UV-Vis spectra recorded during the oxidation of Ph_2CH_2 by $[\text{N4Py}\cdot\text{Fe}^{IV}(\text{O})]^{2+}$. The faster absorbance decrease at $\lambda = 695$ nm ($\tau_{1/2} = 38$ s) compared to the slower increase at $\lambda = 513$ nm ($\tau_{1/2} = 54$ s) supports the presence of a third species (Fig. 3b, right panel). Also in this case the statistical tests were performed on the UV-Vis reaction data. The presence of an elbow in the scree plot curve separating the singular values associated to the third and fourth components (Fig. 2b), and the fact that the IE-function is minimized by N = 3 (Fig. 2d) indicate that there are three active species in the reaction data mixture. Such hypothesis is further corroborated by the absence of an isosbestic point in the UV-Vis spectra for the reaction of Ph_2CH_2 and its presence in the spectral data for the reaction of DHA, as shown in Figs. 1b and 3b.

The EDXAS simultaneous experiment was employed to shed light on the underlying mechanisms and to quantitatively characterize the structures of the intermediates. Fig. 4 presents the EDXAS experimental measurements, while Fig. S1 presents the same EDXAS data where a constant energy cut (white dashed line) starting from the absorbance maximum of the first EDXAS spectrum (for both chemical reactions) was drawn, together with the evolution of all the spectral maxima (blue full line). One may see from Fig. S1 that the EDXAS spectra, for both the DHA and Ph_2CH_2 reactions, shift to lower energies over time, due to the Fe^{IV} reduction. Interestingly, from this qualitative analysis it appears that in the case of the DHA process this shift is continuous from reaction start, whereas for the Ph_2CH_2 oxidation the shift is very slow until t $\sim$ 100 s and then becomes more evident. These differences can be ascribed to the formation of Fe^{III} at the beginning of the Ph_2CH_2 oxidation, whose effect would be to slow down the spectral edge shifts to lower energies if compared to the DHA process where there is no buildup of the Fe^{III} species.

In order to obtain insights into the different mechanisms in place for the

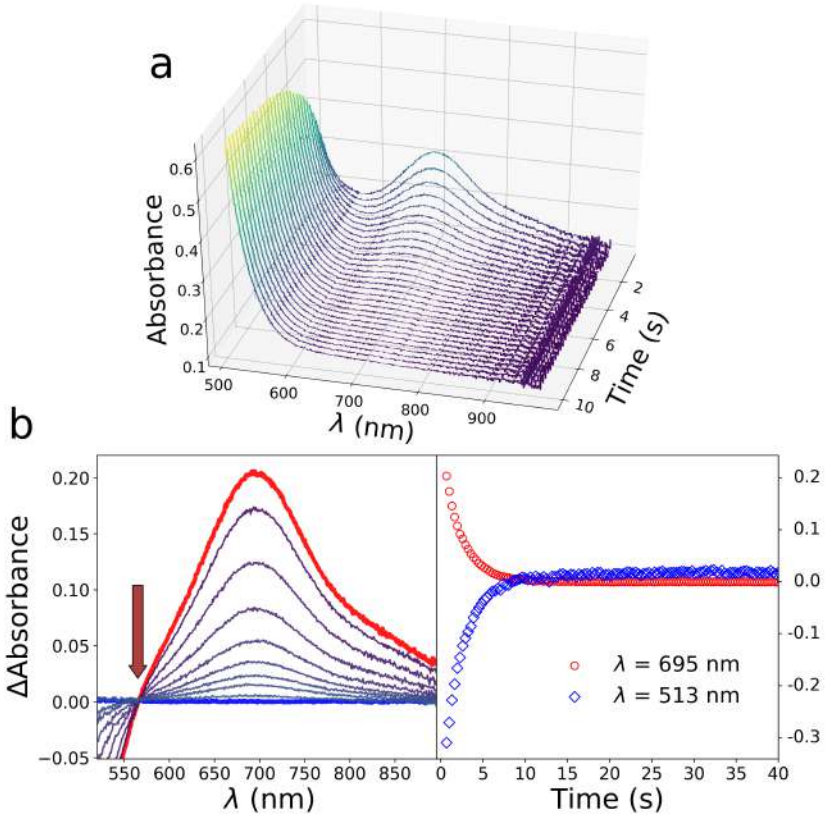

Figure 1: UV-Vis monitoring of the reaction of $[\text{N4Py}\cdot\text{Fe}^{IV}(\text{O})]^{2+}$ (8 mM) with DHA (45 mM) in CH_3CN at 25 °C. (a) Time evolution of selected UV-Vis spectra from reaction start. (b, left panel) Changes in the UV–Vis spectra, where the first and last reaction spectra are depicted in red and blue, respectively. An arrow indicates the isosbestic point's presence. (b, right panel) Time course monitoring at $\lambda = 695$ nm and $\lambda = 513$ nm.

two processes, the UV-Vis data of both reactions were decomposed into the spectra of the reaction components and into their relative concentrations through the transformation matrix approach described in Section 2.1.[18] Fig. 5a and b shows the isolated UV-Vis spectra and fractional concentrational profiles relative to the oxidation of the DHA substrate. The first UV-Vis spectrum (red line in Fig. 5a) belongs to complex $[\text{N4Py}\cdot\text{Fe}^{IV}(\text{O})]^{2+}$ with the characteristic absorbance maximum located at $\lambda = 695$ nm. The second spec-

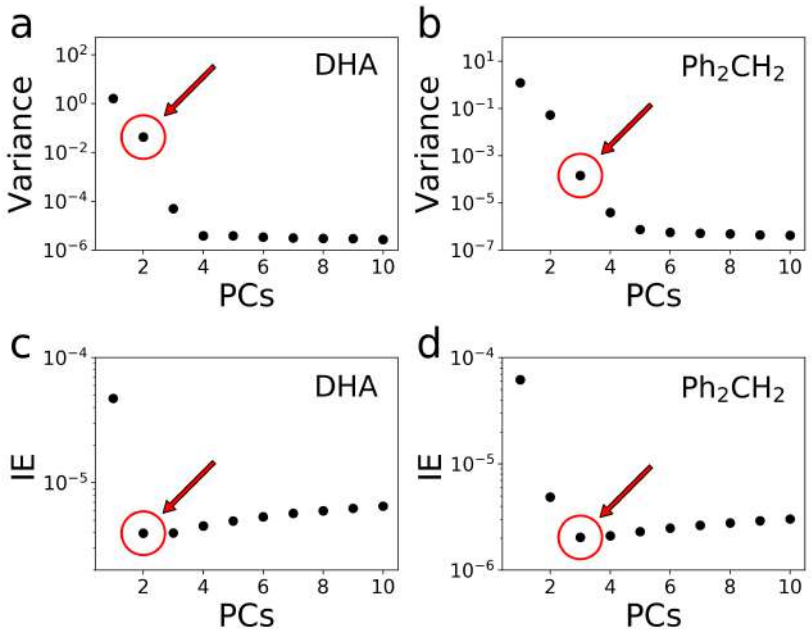

Figure 2: Statistical analysis results. Scree plot and IE-function test for the UV-Vis reaction spectra involving DHA (panels a and c, respectively) and Ph_2CH_2 (panels b and d, respectively). A red arrow indicates the number of principal components necessary to reproduce the UV-Vis datasets suggested by each statistical test.

trum (blue line in Fig. 5a) is assigned to complex $[\text{N4Py}\cdot\text{Fe}^{II}(\text{CH}_3\text{CN})]^{2+}$, a species known to have an absorption maximum at $\lambda = 450$ nm. The isolated spectra are in perfect agreement with those belonging to the pure species, shown in Fig. S6.

The concentration profiles extracted from the UV-Vis data (Fig. 5b) have been employed as mathematical constraints for the analysis of the EDXAS reaction spectra shown in Fig. 4a. For the Lambert-Beer law,[18] the two reaction components contribute to each experimental EDXAS spectrum registered at time t with their own EDXAS spectra weighted for their relative concentration. As a consequence, one can write the matrix of the experimental EDXAS spectra $\boldsymbol{D}_{DHA}$ as:

$$\boldsymbol{D}_{DHA} = \boldsymbol{S}_{DHA} \cdot \boldsymbol{C}_{DHA} + \boldsymbol{E} \tag{7}$$

where every column of $\boldsymbol{D}_{DHA}$ is an EDXAS experimental spectrum for the

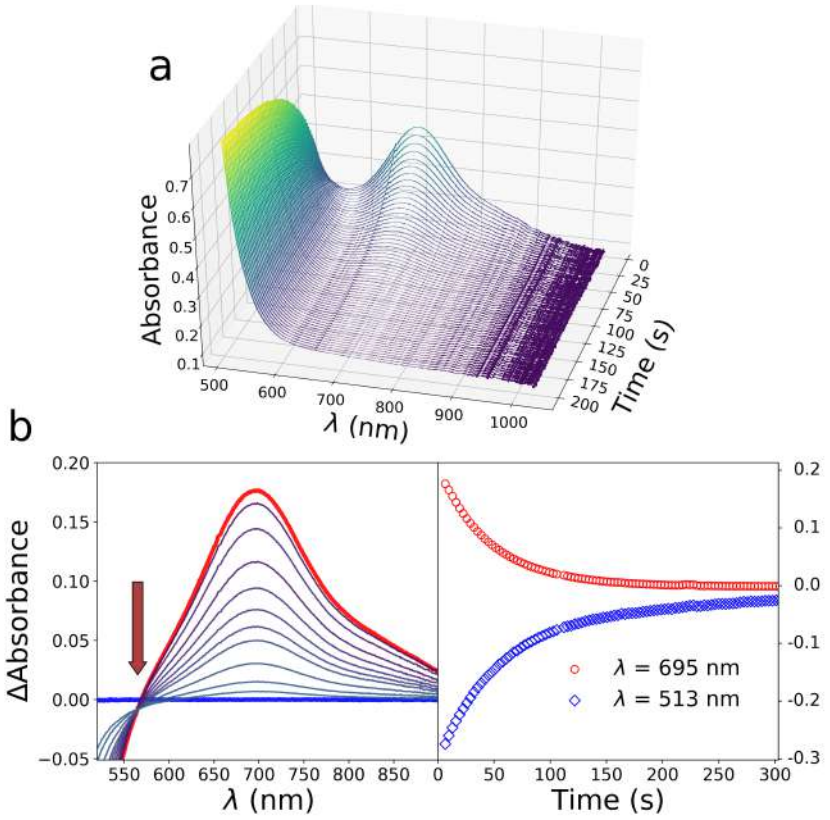

Figure 3: UV-Vis monitoring of the reaction of $[\text{N4Py}\cdot\text{Fe}^{IV}(\text{O})]^{2+}$ (8 mM) with Ph_2CH_2 (300 mM) in CH_3CN at 25 °C. (a) Time evolution of selected UV-Vis spectra from reaction start. (b, left panel) Changes in the UV–Vis spectra, where the first and last reaction spectra are depicted in red and blue, respectively. An arrow indicates the isosbestic point's absence. (b, right panel) Time course monitoring at $\lambda = 695$ nm and $\lambda = 513$ nm.

DHA oxidation, matrices $\boldsymbol{S}_{DHA}$ and $\boldsymbol{C}_{DHA}$ contain on their columns and rows, respectively, the XANES spectral and concentration profiles belonging to $[\text{N4Py}\cdot\text{Fe}^{IV}(\text{O})]^{2+}$ and to $[\text{N4Py}\cdot\text{Fe}^{II}(\text{CH}_3\text{CN})]^{2+}$, while $\boldsymbol{E}$ is the residuals matrix.[38] Since the concentration matrix $\boldsymbol{C}_{DHA}$ is available from the decomposition of the UV-Vis data, matrix $\boldsymbol{S}_{DHA}$ may be recovered as:

$$\boldsymbol{S}_{DHA} = \boldsymbol{D}_{DHA} \cdot \boldsymbol{C}_{DHA}^{T} \cdot (\boldsymbol{C}_{DHA} \cdot \boldsymbol{C}_{DHA}^{T})^{-1} \tag{8}$$

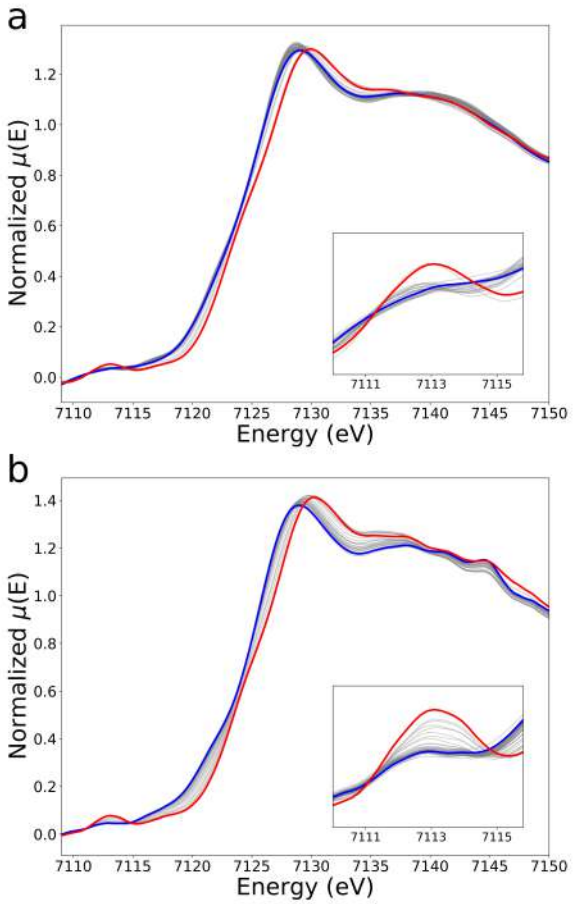

Figure 4: Time evolution of the Fe K-edge EDXAS spectra of the oxidations of DHA (a) and Ph_2CH_2 (b) by $[N4Py{\cdot}Fe^{IV}(O)]^{2+}$ in CH_3CN at °C. The first and last reaction spectra are depicted in red and blue, respectively. A magnification of the characteristic 1s→3d dipole-forbidden transition region is shown in the insets of both panels.

where $\boldsymbol{C}_{DHA}^{T}$ denotes the transpose of $\boldsymbol{C}_{DHA}$. Matrix $\boldsymbol{E}$ contained in Equation 7 is minimized by refining the spectra $\boldsymbol{S}$ of eq. 8.
The obtained XANES spectra are presented in Fig. 5c and are assigned to $[N4Py{\cdot}Fe^{IV}(O)]^{2+}$ (red line in Fig. 5c) and to $[N4Py{\cdot}Fe^{II}(CH_3CN)]^{2+}$ (blue line in Fig. 5c). The energy position of the main absorption edge unambiguously identifies the oxidation state of each spectral component. In fact, the first inflection points of the spectra belonging to the Fe^{IV} initial

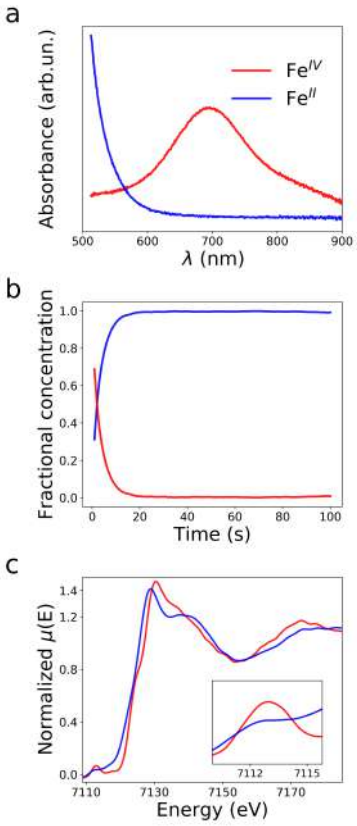

Figure 5: UV-Vis spectra (a) and fractional concentration profiles (b) obtained through the matricial decomposition of the UV-Vis data for the DHA oxidation. The UV-Vis spectra in panel (a) are on the same scale. (c) Fe K-edge XANES spectra derived through matricial division and assigned to the two reaction key species (the region of the characteristic 1s→3d dipole-forbidden transition is shown in the inset).

species and to the Fe^{II} product lie at higher and lower energies, respectively. The identification of the Fe^{IV} spectrum is further strengthened by the presence of a characteristic 1s→3d transition centered at approximately 7113 eV (see inset in Fig. 5c). In fact, it is well established that, because of their non-centrosymmetry, Fe^{IV}-oxo complexes including $[N4Py{\cdot}Fe^{IV}(O)]^{2+}$ possess relatively intense 1s→3d transitions.[39,40]

In the case of the Ph_2CH_2 oxidation, both the UV-Vis and the EDXAS reaction data were subjected to independent transformation matrix decomposi-

tions into the spectral and concentration profiles of the three main reaction components.

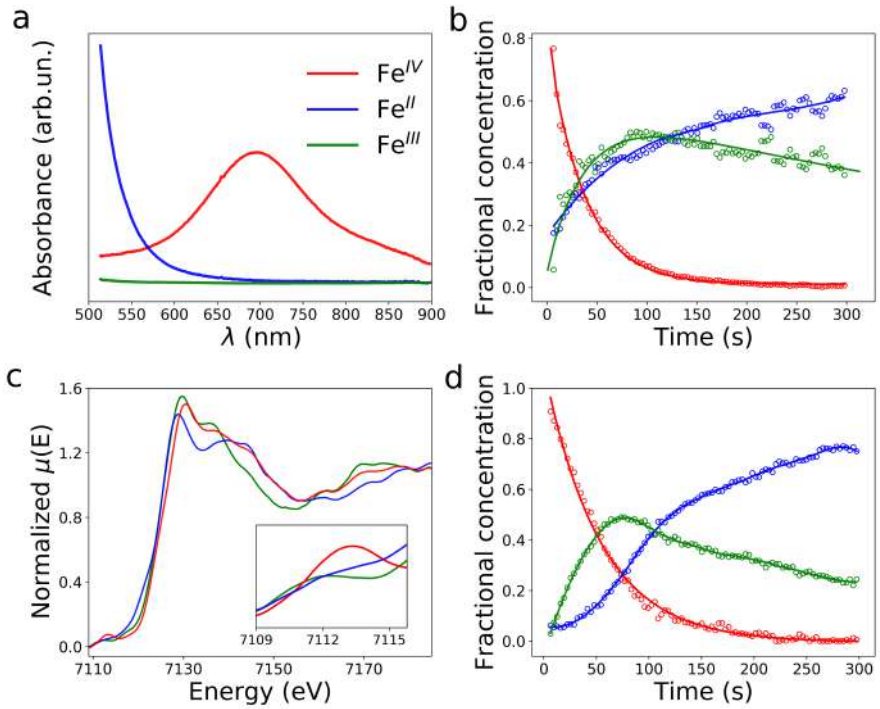

Figure 6: Results of the MCR decomposition applied to the spectra for the Ph_2CH_2 reaction. UV-Vis and XANES extracted spectra assigned to the reaction key species (panels (a) and (c), respectively) and associated concentration profiles (panels (b) and (d), respectively). The UV-Vis spectra in panel (a) are on the same scale. The dotted lines in panel (d) constitute the concentrations obtained through the decomposition of the UV-Vis and EDXAS reaction data, while the full lines are meant to aid in the visualization.

The results of the decomposition of the UV-Vis data are shown in Fig. 6a,b. The first spectrum (red line in Fig. 6a) and second spectrum (blue line in Fig. 6a) are assigned to complexes $[\text{N4Py}\cdot\text{Fe}^{IV}(\text{O})]^{2+}$ and $[\text{N4Py}\cdot\text{Fe}^{II}(\text{CH}_3\text{CN})]^{2+}$, respectively. The third extracted spectral component (green line in Fig. 6a), having a very low signal, is identified as belonging to $[\text{N4Py}\cdot\text{Fe}^{III}(\text{OH})]^{2+}$. In fact, it is known that this species exhibits a very weak UV-Vis absorbance, if any, in the investigated spectral region.[2,35] This hypothesis is supported by

the associated extracted concentration profiles for the three reaction species, presented in Fig. 6b. The concentrations of the Fe^{IV} initial species and Fe^{II} product decay and increase, respectively, while that of the Fe^{III} intermediate increases to reach a maximum before decaying towards what appears to be a constant value.
The extracted XANES spectra and fractional concentration profiles belonging to the three reaction key species are presented in Fig. 6c,d. The spectral component whose inflection point lies at the highest energy (red line in Fig. 6c) is assigned to complex $[N4Py{\cdot}Fe^{IV}(O)]^{2+}$. The spectra whose main absorption edges lie at the lowest (blue line in Fig. 6c) and intermediate (green line in Fig. 6c) energies are assigned to complexes $[N4Py{\cdot}Fe^{II}(CH_3CN)]^{2+}$ and $[N4Py{\cdot}Fe^{III}(OH)]^{2+}$, respectively. Notably, the correct identification of the Fe^{IV} and Fe^{II} species is further confirmed by the presence of the characteristic 1s→3d transition in the Fe^{IV} spectrum (see inset in Fig. 6c), and by the near equivalence of the Fe^{IV} and Fe^{II} spectra with the spectra of $[N4Py{\cdot}Fe^{IV}(O)]^{2+}$ and $[N4Py{\cdot}Fe^{II}(CH_3CN)]^{2+}$, respectively, derived from the DHA reaction data (Figs. 5c and 6c). The dipole-forbidden transition is weak and centered at approximately 7112 eV in the spectrum of the Fe^{III} compound, because of the lower oxidation state.
The fractional concentration extracted from the analysis of the EDXAS data (see Fig. 6d) for the Fe^{IV} initial species exponentially decays to zero, while that of the Fe^{II} species increases. Conversely, the concentration of the Fe^{III} component increases to reach a maximum between t = 50 s and t = 90 s and then slowly decreases towards a plateau.[41]

Altogether the results obtained from the combined XAS/UV-Vis analysis indicate that a different reaction path exists for the two investigated reactions. In the case of DHA the Fe^{IV} initial species is directly converted into the Fe^{II} product, while in the case of Ph_2CH_2 an intermediate Fe^{III} complex is formed.To have a further proof of this finding ferrocene (Fc) has been added at the reaction end. In the case of Ph_2CH_2 addition of Fc causes an increase of the absorbance at $\lambda = 450$ nm, ascribed to the $Fe^{III} \rightarrow Fe^{II}$ reduction while, on the other hand, performing the same procedure on the DHA reaction mixture produces no significant increase in the Fe^{II} UV-Vis absorption band, thus confirming the previous results (see Section 2.4 of ESI). These findings differ from those previously reported in the literature, where it was found that Fe^{III} represents a major reaction product in the reaction of DHA with $[N4Py{\cdot}Fe^{IV}(O)]^{2+}$ employing iodosobenzene to generate the Fe^{IV}-oxo complex.[2] Conversely, in our experimental conditions due to

the generation of the Fe^{IV}-oxo complex through AcOOH in acetic acid, acid species such as AcOH and AcOOH are present in the reaction mixture which may increase the redox potential of the Fe^{III}-OH complex and render it capable of oxidizing in a very fast process the DHA radical to the DHA cation, yielding Fe^{II} straight away. The increased reactivity of the Fe^{III} hydroxide under our reaction conditions would be enough to oxidize the DHA radical, since the formation of the cation would benefit from the driving force of its re-aromatization to anthracene. Conversely, the oxidation of the diphenylmethyl radical would yield a dibenzylic cation that would not possess the same driving force. Indeed, the percentages of Fe^{III} and Fe^{II} produced in the reaction of Ph_2CH_2 with $[N4PyFe^{IV}(O)]^{2+}$ generated by reaction of the Fe^{II} complex with AcOOH in our conditions (66% of Fe^{III} and 34% of Fe^{II}) are lower and higher, respectively, than those observed by carrying out the reaction in the conditions employed by Nam *et al.*,[2] with the Fe^{IV}-oxo complex generated by reaction with PhIO (73% for Fe^{III} and 27% for Fe^{II}).[42] Interestingly, the concentration of the Fe^{III} component, towards the end of the reactive process, appears to approach a constant value, in combination with that of the Fe^{II} product. This finding, together with the fact that the concentration of the Fe^{III} complex is non-zero at reaction end as verified through the addition of Fc, suggests that the Fe^{III}-OH species is in part converted to Fe^{II} by reducing species formed as the reaction proceeds, such as hydroperoxides. Overall, the concentration profiles extracted through the EDXAS data (Fig. 6d) and the UV-Vis data (Fig. 6b) share a high degree of similarity. Solely small differences occur whose origin may be assigned to the larger experimental noise affecting the XANES data and to a certain amount of rotational ambiguity due to the use of the transformation matrix approach.[18] Such rotational ambiguity may also account for the small underestimation of the Fe^{III}/ Fe^{II} product ratio determined by the multivariate decomposition of the coupled EDXAS/UV-Vis data if compared to that assessed through the addition of Fc to the reaction mixture (which is approximately equal to 2, see Fig. S3), together with the non-quantitative nature of the latter method.

The mechanistic implications of these results may be rationalized as shown in Fig. 7. In the case of DHA, the initial HAT from the Fe^{IV}-oxo complex is followed by a fast ET (Fig. 7 a, step a) to produce the Fe^{II} complex with little or no accumulation of the Fe^{III} oxidation state and a cation which likely undergoes a fast deprotonation (desaturation/aromatization process) to produce anthracene.[43] In the case of Ph_2CH_2 the HAT is slower and followed

by a radical dissociation step (Fig. 7 b, step b) leading to a diphenylmethyl radical which can be likely oxidized to the corresponding cation precursor of the hydroxylation product Ph_2CHOH and the accumulation of the Fe^{III} complex whose concentration is partly depleted upon reduction to Fe^{II} (Fig. 7 b, step c).[44] On the basis of such framework, we suggest that the active third species (other than the initial Fe^{IV} and final Fe^{II} complexes) may be identified as $[N4Py{\cdot}Fe^{III}(OH)]^{2+}$.

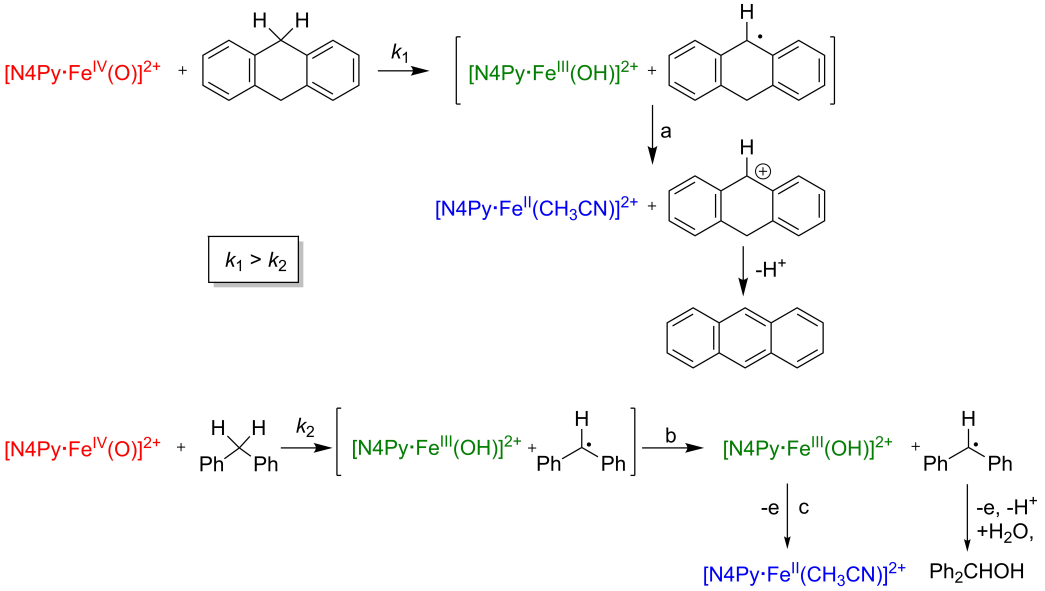

Figure 7: Proposed mechanisms for the investigated reactions. Upper part: (a) electron transfer from the radical to $[N4Py{\cdot}Fe^{III}(OH)]^{2+}$. Lower part: (b) escape of the radical from the ion cage; (c) reduction of $[N4Py{\cdot}Fe^{III}(OH)]^{2+}$ to $[N4Py{\cdot}Fe^{II}(CH_3CN)]^{2+}$.

In order to obtain detailed structural information for the reaction intermediates and to confirm their proposed chemical identification, a full multiple scattering (MS) analysis was performed for the XANES spectra isolated from the EDXAS dataset relative to the Ph_2CH_2 oxidation (see Section 2.7 of ESI).[48–52] In the case of the Fe^{IV} and Fe^{III} species, the iron first coordination shell is made up by the four nitrogen atoms belonging to the N4Py backbone (N_{Py}), by one nitrogen atom bound to three carbon atoms (N_{amine}) and by an oxygen atom. Conversely, in the Fe^{II} complex the iron metal cation is coordinated by the four N_{Py} atoms, by a single N_{amine} atom and by a

	Fe-N_{amine}		Fe-N_{Py}		Fe-N_{ACN}		Fe-O	
	N	r(Å)	N	r(Å)	N	r(Å)	N	r(Å)
Fe^{IV}								
Cryst.[45,46]	1	2.033(8)	4	1.957(5)	-	-	1	1.639(5)
EXAFS[39]	-	-	4	1.96	-	-	1	1.64
This work	1	2.08(5)	4	2.01(5)	-	-	1	1.69(5)
Fe^{III}								
This work	1	1.97(5)	4	2.10(5)	-	-	1	1.89(5)
Fe^{II}								
Cryst.[47]	1	1.961(3)	4	1.967(3) - 1.976(3)	1	1.915(3)	-	-
This work	1	1.98(5)	4	1.98(5)	1	1.96(5)	-	-

Table 1: Fe K-edge XANES structural parameters of the [N4Py·Fe^{IV}(O)]$^{2+}$ (Fe^{IV}), [N4Py·Fe^{III}(OH)]$^{2+}$ (Fe^{III}) and [N4Py·Fe^{II}(CH_3CN)]$^{2+}$ (Fe^{II}), complexes compared to available literature crystallographic and EXAFS data. N is the number of coordinating atoms. $R_{Fe-N_{amine}}$ and $R_{Fe-N_{Py}}$ are the average distances between the metal cation and the single tertiary nitrogen atom and the four secondary nitrogen atoms of the N4Py molecule, respectively, $R_{Fe-N_{ACN}}$ is the distance between the metal cation and the nitrogen solvent atom while R_{Fe-O} is the distance between the metal cation and the coordinating oxygen atom . In all cases, except for the crystal data reported in Ref.,[47] the average Fe-N_{Py} distance is presented. The errors affecting the listed distances are enclosed by parentheses.

CH_3CN solvent nitrogen atom (N_{ACN}). A fitting procedure for the Fe^{IV} and Fe^{II} extracted XANES components has been performed by optimizing the nonstructural parameters while the Fe–N_{Py}, the Fe–N_{amine}, the Fe–O and the Fe–N_{ACN} distances were allowed to vary within ±0.05 Å of the crystallographic ones. Conversely, in the case of the Fe^{III} complex, the Fe–ligand distances were refined together with the nonstructural parameters during the fitting. The best-fit results are shown in Fig. S7 along with the associated molecular clusters. Overall, the agreement between the theoretical spectra and the isolated components is very good. The structural parameters are listed in Table 1, while the full list of the nonstructural parameters together with the residual error R_{sq} are reported in Table S1.

One may note that for the Fe^{III} complex the Fe-N_{amine} and Fe-N_{Py} distances are equal to 1.97(5) Å and 2.10(5) Å, respectively, while the calculated Fe-O distance is 1.89(5) Å, a value that differs from the Fe-O distance of 1.69(5) Å simulated for the Fe^{IV} complex. The reported bond lenghts for the Fe^{III}-OH intermediate are higher than the average Fe-N distance of 1.99 Å and the Fe-O distance of 1.81 Å evaluated using DFT-based calculations.[2] Conversely, the average Fe-N_{Py} distance of 2.10(5) Å refined here for $[N4Py{\cdot}Fe^{III}(OH)]^{2+}$ is very similar to the average Fe-N_{Py} distances present in the crystal structure of complex $[N4Py{\cdot}Fe^{III}(OCH_3)]^{2+}$, where a methoxy group coordinates the iron site. Indeed in this structure the two distinct cations that comprise the asymmetric unit have Fe-N_{amine}, Fe-O and average Fe-N_{Py} distances of 2.198(3) Å, 1.772(3) Å and 2.11(2) Å, and of 2.100(3) Å, 1.789(3) Å and 2.05(2) Å, respectively.[53] Additionally, in the crystal structure of complex $[Fe^{III}(OH)(N4Py^{2NpNH}][OTf]_2$ a Fe-O distance equal to 1.837(3) Å has been reported, a value that is in line with the Fe-O distance of 1.89(5) Å we have obtained.[54] Finally, it is of note that the Fe-N_{Py}, Fe-N_{amine}, Fe-O and Fe-N_{ACN} distances presented in this work for the Fe^{IV}, Fe^{III} and Fe^{II} complexes are identical within statistical errors to the same distances evaluated for these complexes, as determined by a multivariate and theoretical analysis of EDXAS data for the oxidation of *para*-methoxythioanisole by $[N4Py{\cdot}Fe^{IV}(O)]^{2+}$ in CH_3CN at room temperature and in the presence of AcOOH and AcOH.[33]

4 Conclusions

In this work it is shown through a combined spectroscopic, multivariate statistical and theoretical investigation that the activation mechanism of C-H bonds by a nonheme Fe^{IV}-oxo complex differs depending on the employed hydrocarbon substrate. In particular, we suggest that $[N4Py{\cdot}Fe^{IV}(O)]^{2+}$ oxidizes Ph_2CH_2 through a HAT-RD mechanism in which Fe^{III} is formed both as a reaction intermediate and a product. By contrast, we find that in the oxidation of DHA a HAT-ET mechanism is in place without the accumulation of Fe^{III}. Through a direct analysis of the time-resolved coupled EDXAS/UV-Vis reaction spectra collected at room temperature and by performing a quantitative analysis of the extracted XANES spectra of the key reaction components, we acquire mechanistic information on the process and we structurally characterize all reaction intermediates. The implemented strategy can be useful in the future to gain further insight into the mechanisms of complex reactive processes involving organic substrates.

Conflicts of interest

There are no conflicts to declare.

Acknowledgments

The ESRF synchrotron radiation facility is acknowledged for the provision of beamtime for time-resolved XAS (ID24). We acknowledge financial support from the Italian Ministry of University and Research (MIUR) through grant "PRIN 2017, 2017KKP5ZR, MOSCATo" and from University of Rome La Sapienza grant n. RG11916B702B43B9.

References

[1] W. Nam, *Acc. Chem. Res.*, 2007, **40**, 522–531.

[2] K.-B. Cho, X. Wu, Y.-M. Lee, Y. H. Kwon, S. Shaik and W. Nam, *J. Am. Chem. Soc.*, 2012, **134**, 20222–20225.

[3] P. Ortiz de Montellano, *Cytochrome P450: Structure, Mechanism, and Biochemistry: Third edition*, 2005, 1–689.

[4] S. Shaik, D. Kumar, S. P. de Visser, A. Altun and W. Thiel, *Chem. Rev.*, 2005, **105**, 2279–2328.

[5] C. Krebs, D. G. Fujimori, C. T. Walsh and J. M. Bollinger, *Acc. Chem. Res.*, 2007, **40**, 484–492.

[6] J. Kaizer, E. J. Klinker, N. Y. Oh, J.-U. Rohde, W. J. Song, A. Stubna, J. Kim, E. Münck, W. Nam and L. Que, *J. Am. Chem. Soc.*, 2004, **126**, 472–473.

[7] H. Hirao, D. Kumar, L. Que and S. Shaik, *J. Am. Chem. Soc.*, 2006, **128**, 8590–8606.

[8] C. Geng, S. Ye and F. Neese, *Angew. Chem. Int. Ed.*, 2010, **49**, 5717–5720.

[9] A. Mukherjee, M. Martinho, E. L. Bominaar, E. Münck and L. Que Jr., *Angew. Chem. Int. Ed.*, 2009, **48**, 1780–1783.

[10] M. Bigi, S. Reed and S. White, *Nat. Chem.*, 2011, **3**, 216.

[11] D. Usharani, D. Janardanan and S. Shaik, *J. Am. Chem. Soc.*, 2011, **133**, 176–179.

[12] A. Company, I. Prat, J. R. Frisch, D. R. Mas-Ballesté, M. Güell, G. Juhsz, X. Ribas, D. E. Münck, J. M. Luis, L. Que Jr. and M. Costas, *Chemistry - A European Journal*, 2011, **17**, 1622–1634.

[13] X. Wu, M. S. Seo, K. M. Davis, Y.-M. Lee, J. Chen, K.-B. Cho, Y. N. Pushkar and W. Nam, *J. Am. Chem. Soc.*, 2011, **133**, 20088–20091.

[14] G. Olivo, A. Barbieri, V. Dantignana, F. Sessa, V. Migliorati, M. Monte, S. Pascarelli, T. Narayanan, O. Lanzalunga, S. Di Stefano and P. D'Angelo, *J. Phys. Chem. Lett.*, 2017, **8**, 2958–2963.

[15] G. Capocasa, F. Sessa, F. Tavani, M. Monte, G. Olivo, S. Pascarelli, O. Lanzalunga, S. Di Stefano and P. D'Angelo, *J. Am. Chem. Soc.*, 2019, **141**, 2299–2304.

[16] F. Tavani, A. Martini, G. Capocasa, S. Di Stefano, O. Lanzalunga and P. D'Angelo, *Inorg. Chem.*, 2020, **59**, 9979–9989.

[17] F. Tavani, A. Martini, F. Sessa, G. Olivo, G. Capocasa, O. Lanzalunga, S. Di Stefano and P. D'Angelo, *Phys. Conf. Series*, 2020, submitted.

[18] A. Martini, S. Guda, A. Guda, G. Smolentsev, A. Algasov, O. Usoltsev, M. Soldatov, A. Bugaev, Y. Rusalev, C. Lamberti and A. Soldatov, *Comput. Phys. Comm.*, 2019, 107064.

[19] O. Kleifeld, A. I. Frenkel, J. Martin and I. Sagi, *Nat. Struct. Mol. Biol.*, 2003, **10**, 98–103.

[20] A. Solomon, B. Akabayov, A. Frenkel, M. E. Milla and I. Sagi, *PNAS*, 2007, **104**, 4931–4936.

[21] G. Smolentsev, G. Guilera, M. Tromp, S. Pascarelli and A. V. Soldatov, *J. Chem. Phys.*, 2009, **130**, 174508.

[22] P. Conti, S. Zamponi, M. Giorgetti, M. Berrettoni and W. H. Smyrl, *Anal. Chem.*, 2010, **82**, 3629–3635.

[23] H. W. Carvalho, S. H. Pulcinelli, C. V. Santilli, F. Leroux, F. Meneau and V. Briois, *Chem. Mater.*, 2013, **25**, 2855–2867.

[24] A. Martini, E. Alladio and E. Borfecchia, *Top. Catal.*, 2013, **61**, 1296–1407.

[25] A. Martini, E. Borfecchia, K. A. Lomachenko, I. A. Pankin, C. Negri, G. Berlier, P. Beato, H. Falsig, S. Bordiga and C. Lamberti, *Chem. Sci.*, 2017, **8**, 6836–6851.

[26] A. Voronov, A. Urakawa, W. van Beek, N. E. Tsakoumis, H. Emerich and M. R, *Anal. Chim. Acta*, 2014, **840**, 20–27.

[27] W. H. Cassinelli, L. Martins, A. R. Passos, S. H. Pulcinelli, C. V. Santilli, A. Rochet and V. Briois, *Catal. Today*, 2014, **229**, 114 – 122.

[28] A. Rochet, B. Baubet, V. Moizan, C. Pichon and V. Briois, *C. R. Chim.*, 2016, **19**, 1337 – 1351.

[29] A. Rochet, B. Baubet, V. Moizan, E. Devers, A. Hugon, C. Pichon, E. Payen and V. Briois, *J. Phys. Chem. C*, 2017, **121**, 18544–18556.

[30] M. Fernandez-Garcia, C. Marquez Alvarez and G. L. Haller, *J. Phys. Chem.*, 1995, **99**, 12565–12569.

[31] B. L. Caetano, V. Briois, S. H. Pulcinelli, F. Meneau and C. V. Santilli, *J. Phys. Chem. C*, 2017, **121**, 886–895.

[32] F. Tavani, M. Fracchia, N. Pianta, P. Ghigna, E. Quartarone and P. D'Angelo, *Chem. Phys. Lett.*, 2020, **760**, 137968.

[33] F. Tavani, G. Capocasa, A. Martini, F. Sessa, S. Di Stefano, O. Lanzalunga and P. D'angelo, *Dalton Trans.*, 2020, accepted, 10.1039/D0DT03083J.

[34] A. Martini and E. Borfecchia, *Crystals*, 2020, **10**, 664.

[35] Y. Nishida, Y. Morimoto, Y.-M. Lee, W. Nam and S. Fukuzumi, *Inorg. Chem.*, 2013, **52**, 3094–3101.

[36] A. Martini, A. A. Guda, S. A. Guda, A. Dulina, F. Tavani, P. D'Angelo, E. Borfecchia and A. Soldatov, *Phys. Conf. Series*, 2020, submitted.

[37] I. Markovsky, *Automatica*, 2008, **44**, 891–909.

[38] C. Ruckebusch and L. Blanchet, *Anal. Chim. Acta*, 2013, **765**, 28–36.

[39] D. Wang, K. Ray, M. J. Collins, E. R. Farquhar, J. R. Frisch, L. Gómez, T. A. Jackson, M. Kerscher, A. Waleska, P. Comba, M. Costas and L. Que, *Chem. Sci.*, 2013, **4**, 282–291.

[40] J.-U. Rohde, S. Torelli, X. Shan, M. H. Lim, E. J. Klinker, J. Kaizer, K. Chen, W. Nam and L. Que, *J. Am. Chem. Soc.*, 2004, **126**, 16750–16761.

[41] The choice of treating separately the UV–Vis and the EDXAS data relative to the Ph_2CH_2 oxidation is mainly due to the high level of noise affecting the retrieved UV-Vis concentration profiles (if compared to those retrieved from the UV-Vis data relative to the oxidation of DHA) whose employment could cause the alteration of the pure XANES spectra retrieved from the EDXAS dataset. Note that this level of noise

is intrinsic in the PCs extracted from the dataset and cannot be removed using any method.

[42] The oxidation experiments were repeated under the same conditions for DHA and Ph_2CH_2: namely, 45 mM substrate concentration and a defect of oxidant (AcOOH 40 mM). Under these conditions only UV-Vis analyses were performed (see ESI, Fig. S5). The Fe(III) percentages were found to be 72% and 11% for Ph_2CH_2 and DHA respectively, thus confirming that the redox potential of the iron(IV)-oxo complex is affected by the acid concentration and that the oxidation of the DHA radical is associated to the Fe(III)-OH reduction (see ESI, page 5).

[43] A. Barbieri, O. Lanzalunga, A. Lapi and S. Di Stefano, *J. Org. Chem.*, 2019, **84**, 13549–13556.

[44] The latter process may be promoted by small amounts of alkylhydroperoxide, Ph_2CHOOH, formed by the competitive reaction of the diphenylmethyl radical with molecular oxygen.

[45] E. J. Klinker, J. Kaizer, W. W. Brennessel, N. L. Woodrum, C. J. Cramer and L. Que Jr., *Angew. Chem. Int. Ed.*, 2005, **44**, 3690–3694.

[46] E. J. Klinker, J. Kaizer, W. W. Brennessel, N. L. Woodrum, C. J. Cramer and L. Que Jr., *Angew. Chem.*, 2005, **117**, 3756–3760.

[47] G. Roelfes, M. Lubben, K. Chen, R. Y. N. Ho, A. Meetsma, S. Genseberger, R. M. Hermant, R. Hage, S. K. Mandal, V. G. Young, Y. Zang, H. Kooijman, A. L. Spek, L. Que and B. L. Feringa, *Inorg. Chem.*, 1999, **38**, 1929–1936.

[48] P. D'Angelo, A. Lapi, V. Migliorati, A. Arcovito, M. Benfatto, O. M. Roscioni, W. Meyer-Klaucke and S. Della-Longa, *Inorg. Chem.*, 2008, **47**, 9905–9918.

[49] G. Salzano, M. Brennich, G. Mancini, T. Tran, G. Legname, P. D'Angelo and G. Giachin, *Biophys. J.*, 2020, **118**, 676–687.

[50] A. Arcovito, T. Moschetti, P. D'Angelo, G. Mancini, B. Vallone, M. Brunori and S. Della Longa, *Arch. Biochem. Biophys.*, 2008, **475**, 7–13.

[51] P. D'Angelo, V. Migliorati, F. Sessa, G. Mancini and I. Persson, *J. Phys. Chem. B*, 2016, **120**, 4114–4124.

[52] E. Burattini, P. D'Angelo, A. Di Cicco, A. Filipponi and N. V. Pavel, *J. Phys. Chem.*, 1993, **97**, 5486–5494.

[53] G. Roelfes, M. Lubben, K. Chen, R. Y. N. Ho, A. Meetsma, S. Genseberger, R. M. Hermant, R. Hage, S. K. Mandal, V. G. Young, Y. Zang, H. Kooijman, A. L. Spek, L. Que and B. L. Feringa, *Inorg. Chem.*, 1999, **38**, 1929–1936.

[54] H. S. Soo, A. C. Komor, A. T. Iavarone and C. J. Chang, *Inorg. Chem.*, 2009, **48**, 10024–10035.

Graphical TOC Entry